Open Access

Catalysis Research

LIDSEN Publishing Inc.

Original Research

Thermokinetic and Thermodynamic Parameters for Catalytic Pyrolysis of Medium Density Fiber over Ni/Beta Zeolite

Mateus Carvalho [1], Ana Paula Oliveira [2], Francieli Mayer [2], Cesário Virgens [3], Maria do Carmo Rangel [1, 2, *]

1. Escola Politécnica , Universidade Federal da Bahia, R. Prof. Aristídes Novis, 2-Federação, Salvador, Bahia, Brazil; E-Mails: carvalho.mateus@ufba.br; mcarmov@ufba.br
2. Instituto de Química, Universidade Federal do Rio Grande do Sul, Av. Bento Gonçalves, 9500 – Agronomia, Porto Alegre, Rio Grande do Sul, Brazil; E-Mails: anapaulasoliv@gmail.com; francimayer@gmail.com; maria.rangel@ufrgs.br
3. Departamento de Ciências Exatas e da Terra, Universidade Estadual da Bahia, R. Silveira Martins, 2071-2095 – Cabula, Salvador, Bahia, Brazil; E-Mail: cvirgens@uneb.br

* **Correspondence:** Maria do Carmo Rangel; E-Mails: mcarmov@ufba.br; maria.rangel@ufrgs.br

Academic Editor: Robert Wojcieszak

Special Issue: Recent Advances in Catalysis for Biomass Conversion

Catalysis Research
2022, volume 2, issue 4
doi:10.21926/cr.2204038

Received: August 31, 2022
Accepted: October 20, 2022
Published: November 02, 2022

Abstract

Catalytic pyrolysis is an attractive alternative for converting biomass into energy and chemicals to replace fossil sources. This has encouraged the search for efficient catalysts that can directly remove oxygenated products during pyrolysis, since they are the main problem in the processing and use of the products obtained. The catalytic and non-catalytic pyrolysis of medium density fiber (MDF) over beta zeolite-supported nickel (3 and 5%) was performed using the biomass/catalyst of 1.0/0.2 ratio. The thermokinetic and thermodynamic parameters were determined using the isoconversional and non-isothermal methods of Flynn-Wall-Ozawa (FWO), Kissinger-Ahakira-Sunose (KAS) and Friedman. In addition, the master plots by the Criado method were used to determine the most suitable theoretical solid-state mechanism. The thermodynamic parameters were also obtained using the Friedman method.

The results showed that the addition of the catalyst decreased the activation energy and affected the initial, final and maximum decomposition temperatures, which was related to the superficial acidic sites of beta zeolite that promote cracking and hydrocracking reactions. Nickel further decreased this parameter due to the activity of this metal in hydrodeoxygenation/deoxygenation, oligomerization and dehydration. The Friedman method provided the best correlation coefficient among the methods and was used to determine the thermodynamic parameters. The results showed that E_a increases in the order: MB3Ni < MB5Ni < MB < M.

Keywords
Beta zeolite; nickel; medium density fiber; catalytic pyrolysis; activation energy

1. Introduction

The growing demand for clean energy and the requirements for sustainability worldwide have led government agencies to adopt stricter laws to minimize the environmental impact of using fossil sources. Therefore, replacing oil gas with renewable sources has been recognized as the most efficient route to decrease greenhouse gas emissions. Among several possibilities proposed, the production of biofuels and biochemicals from biomass has significant advantages because of high availability and low cost, besides being renewable [1-4].

Several thermochemical and biochemical routes have been proposed for producing energy and chemicals from biomass, and pyrolysis is considered one of the most promising processes, because of its flexibility, low cost, and simplicity. In addition, different biomasses can be directly used, avoiding their separation into cellulose, hemicellulose, and lignin. However, when biofuels are desired, a further step is needed to remove the oxygenated compounds from bio-oil [5, 6]. These compounds cause undesirable properties to bio-oil such as high water content (15-25% by weight), low calorific value (22-30 MJ kg^{-1}), high total acidity index (100-200), high viscosity (25-1000 m^2 s^{-1}), high oxygen content (15-30%) and high instability which increase corrosiveness and chemical instability. A more economic and simpler process is to carry out pyrolysis over a catalyst, removing the oxygenated compounds in situ and avoiding the next step [7].

Among the catalysts proposed for pyrolysis, zeolites have been considered as the most efficient ones, due to their high specific surface area, multiple channel system, high acidity and shape selectivity [8]. Beta zeolite, for instance, is highly selective to benzene, toluene, ethylbenzene, and xylenes (BTEX) [9], which are high-value chemicals in several industrial processes [9]. In addition, it has high catalytic activity, selectivity, and resistance to deactivation, in various reactions such as cracking, alkylation and acylation of aromatic hydrocarbons and hydroisomerization of alkanes [10, 11]. Beta zeolite is a high silicon content structure consisting of a 3D channel system with rings of 12 members which results in a large pore crystalline aluminosilicate with hydrothermal stability, high surface acidity and hydrophobicity [12, 13].

Despite its importance, biomass pyrolysis is not completely understood because of the complexity of the biomass matrix and the multiplicity of reactions that can occur during pyrolysis [14, 15]. Furthermore, other factors can affect the process, like intraphase and/or interphase

transport phenomena, particle size and operational parameters such as heating rate, temperature, and type of reactor. The understanding of pyrolysis is fundamental for designing industrial-scale processes and choosing the most suitable catalyst to obtain commercially valuable products[16]. To better understand pyrolysis, two strategies are generally adopted: the prediction of the pathway reaction by monitoring and quantifying the products and the determination of the thermokinetic and thermodynamic parameters [17].

Several techniques can be used for the determination of kinetic parameters from non-isothermal thermogravimetric analysis, such as isoconversional fit and free models, which provide information related to the energy required for the pyrolysis reaction in a temperature range [18]. Isoconversional fit models use a single heating rate while free models calculate the thermokinetic parameters from curves obtained at different heating rates [16]. Isoconversional fit methods assume that the entire process can be simplified to a single-step equation without the need for analysis of intermediate processes. These models have been used for studying pyrolysis. For instance, Volli *et al.* (2021) used the Friedman differential isoconversional free model to determine the kinetic parameters of agricultural residues (sawdust, black tea, barley, bagasse, rice husk, and corncob), during non-catalytic pyrolysis [19]. Carvalho *et al.* (2020) used the Friedman model to predict the effect of alkaline treatment on *Pachira aquatica* A. biomass [20] and Castro *et al.* (2020) used both model-free (Friedman) and model-fit (Criado) to study the effect of chemical pre-treatment on the behavior of pseudo-components of *Nephelium lappaceum* L [21]. All these values are needed to simulate and design industrial processes, therefore, making the experimental research of great importance [16]. In this study, the thermokinetic parameters of residues of medium density fiber (MDF) of pyrolysis over beta zeolite-supported nickel were determined by Flynn-Wall-Ozawa (FWO), Kissinger-Akahira-Sunose (KAS) and Friedman isoconversional methods. In addition, the Criado method was used to identify the theoretical solid-state reaction mechanism that best fits the data.

This study intends to fit the lack of understanding of catalytic MDF pyrolysis. To the best of our knowledge, no thermokinetic study has been performed concerning MDF decomposition over beta zeolites. The study will provide a deeper understanding of the role of the catalyst in affecting the reaction network, thermokinetic and thermodynamic parameters during pyrolysis.

2. Materials and Methods

2.1 Biomass Pretreatment

The method of pre-treatment, as well as the chemical composition of MDF residues (M sample) were described in previous work [9]. Before the pyrolysis experiments, the pretreated biomass was dried at 40°C for 12 h and the particles ranging in size from 0.25 to 0.43 mm (40-60 mesh) were selected for the experiments.

2.2 Catalyst Preparation

Beta zeolite was prepared according to the methodology described by Vaudry [22], with some modifications. In brief, silica is extracted from coal ash obtained from a thermoelectric plant. The amount of silica in each coal ash batch (received from the plant) was determined to obtain the same Si/Al molar ratio by different preparations. The gel composition obtained was 1.5 Na_2O/1Al_2O_3/30

SiO_2/8.4 TEAOH/315 H_2O, where TEAOH was tetraethylammonium hydroxide. The sample was ion-exchanged using ammonium nitrate at 80°C for 3 h. The beta zeolite acidic form (B) was impregnated with a nickel nitrate solution to get solids with 3% and 5% w/w, which were dried at 110°C for 24 h and heated (2°C min^{-1}) to 550°C, being kept at this temperature for 5 h. The catalysts were named B3Ni and B5Ni according to nickel concentration in the solids.

2.3 Catalyst Characterization

The characteristic structure of zeolite beta in the samples was confirmed through X-ray diffraction. The experiments were carried out in an Ultima IV model Rigaku equipment, using CuKα radiation generated at 40 kV and 17 mA and a monochromator. The analysis was performed in a 2 θ scan range from 5° to 50°, with a goniometer speed of 3°·min^{-1}. The chemical analysis of the samples was carried out by the Flame Atomic Absorption Spectrometry - FAAS technique in an AAnalyst 200 model Perkin-Elmer equipment. A hollow cathode lamp (LUMINATM Hollow Cathode Lamp - Perkin-Elmer) was used. Specific surface area and porosity measurements of the catalysts were performed through nitrogen adsorption/desorption, at 77 K, in a TriStart II 3020 model Micromeritics equipment.

2.4 Biomass/Catalyst Ratio

To compare the activity of the catalysts, pure beta zeolite was evaluated besides beta zeolite supported nickel (3% and 5%). Moreover, MDF non-catalytic pyrolysis was also performed. The biomass (M) and the catalyst (1/0.2) were mixed to produce MB, MB3Ni (3% Ni) and MB5Ni (5% Ni) samples.

2.5 Thermogravimetric Analysis

The MDF pyrolysis was carried out on TGA Q50 equipment (V6.7 Build 203, Universal) using approximately 7.0 mg of sample. The oven was heated from 25°C to 900°C at heating rates (β) of 5, 10, 15 and 20°C min^{-1} under nitrogen flow (60 mL min^{-1}). The data obtained by the equipment software were converted into csv files and exported to Excel for calculation.

2.6 Kinetic Analysis

The basis of isoconversional methods is to consider the chemical process as a general, single-step equation which can be described by the fundamental relationship shown in Eq. 1, where *k(T)* is the rate constant, *f(α)* is a function related to the chosen reaction model and α represents the conversion degree. The term α can be calculated as shown in Eq. 2, where m_0 and m_f are the initial and final weight of the sample, respectively, and m_t is the weight at any given time. The rate constant k and its temperature dependency are described by the Arrhenius equation (Eq. 3), where A is the pre-exponential factor, E_a is the activation energy, R is the gas constant, and T is the temperature.

$$\frac{d\alpha}{dt} = k(T)f(\alpha) \quad (1)$$

$$\alpha = \frac{m_0 - m_t}{m_0 - m_f} \tag{2}$$

$$k(T) = A \exp\left(-\frac{E_a}{RT}\right) \tag{3}$$

Eq. (3) defines a basis for using differential kinetic methods that can be applied at any temperature program, isothermal or non-isothermal, relating reaction rate, conversion fraction and temperature [21]. Under non-isothermal conditions, the heating rate (β) can be expressed by Eq. 4, where dT is an infinitesimal temperature change. Substituting the Eq. 3 and 4 into Eq. 1, we get Eq. 5, where *f(α)* is an algebraic equation that can be associated with the physical models that commonly represent the kinetics of solid-state reactions, as described in Table 1.

Table 1 Mathematic expressions for f(α) and g(α) according to different solid-state reaction mechanism models.

Mechanism		***f(α)***	***g(α)***	**Abbreviations**
Power law	Power law. n = ½	$2\alpha^{1/2}$	$\alpha^{1/2}$	P_2
	Power law. n = ⅓	$3\alpha^{2/3}$	$\alpha^{1/3}$	P_3
	Power law. n = ¼	$4\alpha^{3/4}$	$\alpha^{1/4}$	P_4
Chemical Reaction	First-order reaction	$1-\alpha$	$-\ln(1-\alpha)$	F_1
	Second-order reaction	$(1-\alpha)^2$	$(1-\alpha)^{-1}-1$	F_2
	Third-order reaction	$(1-\alpha)^3$	$[(1-\alpha)^{-2}-1]/2$	F_3
	n-order reaction	$(1-\alpha)^n$	$[(1-\alpha)^{-(n-1)}-1]/(n-1)$	Fn
Diffusion reaction	One-dimensional diffusion	0.5α	α^2	D_1
	Two-dimensional diffusion	$[-\ln(1-\alpha)]^{-1}$	$(1-\alpha)\ln(1-\alpha)+\alpha$	D_2
	Three-dimensional diffusional-Jander	$1.5(1-\alpha)^{2/3}[1-(1-\alpha)^{1/3}]^{-1}$	$[1-(1-\alpha)^{1/3}]^2$	D_3
	Three-dimensional Gistling-Brounsthein	$1.5[(1-\alpha)^{-1/3}-1]^{-1}$	$\left(1-\frac{2\alpha}{3}\right)-(1-\alpha)^{2/3}$	D_4
Phase interfacial reaction	One dimension	1	α	R_1
	Two dimensions	$2(1-\alpha)^{1/2}$	$1-(1-\alpha)^{1/2}$	R_2
	Three dimensions	$3(1-\alpha)^{2/3}$	$1-(1-\alpha)^{1/3}$	R_3
Nucleation and growth reaction	Two dimensional	$2(1-\alpha)[-\ln(1-\alpha)]^{1/2}$	$[-\ln(1-\alpha)]^{1/2}$	A_2
	Three-dimensional	$3(1-\alpha)[-\ln(1-\alpha)]^{2/3}$	$[-\ln(1-\alpha)]^{1/3}$	A_3

$$\beta = \frac{dT}{dt} \tag{4}$$

$$\beta\left(\frac{d\alpha}{dT}\right) = Aexp\left(-\frac{E_a}{RT}\right)f(\alpha) \tag{5}$$

Eq. 5 is introduced into the function $g(\alpha) = \int_0^x \frac{d\alpha}{f(\alpha)}$ to obtain Eq. 6.

$$g(\alpha) = \int_0^\alpha \frac{d\alpha}{f(\alpha)} = \int_{T_i}^{T_f} \frac{1}{\beta}\left(Ae^{\frac{-E}{RT}}\right)dT \tag{6}$$

2.6.1 FWO Model

Ozawa [23] and Flynn-Wall [24] independently developed an iso-conversional integral method for non-isothermal data, as shown in Eq. 7.

$$\ln\beta = \ln\left(\frac{AE_a}{Rg(\alpha)}\right) - 5.331 - 1.052\frac{E_a}{RT} \tag{7}$$

In Eq. 7, by plotting of ln(β) vs. 1/T for each conversion degree at several heating ratios, the activation energy can be calculated from the slope of the line, and the pre-exponential factor (A) can be obtained from the y-intercept.

2.6.2 KAS Model

The Kissinger method was developed by Homer E. Kissinger in 1957 [25]. Due to its simplicity and versatility, except that no reaction mechanism is required to determine the kinetic parameters, it became one of the most popular approaches for determining kinetic parameters via thermal analysis [26]. The Kissinger-Akahira- Sunose [27] method is based on Kissinger method and allows the calculation of activation energy and frequency factor as shown in Eq. 8.

$$\ln\left(\frac{\beta}{T^2}\right) = \ln\left(\frac{RA}{g(\alpha)E_a}\right) - \frac{E_a}{RT} \tag{8}$$

2.6.3 Friedman Model

Friedman method [28] is a differential isoconversional model used to determine the activation energy (E_a) and the frequency factor (A). It is derived directly from Eq. 5, applying the natural logarithm as shown in Eq. 9.

$$\ln\left(\beta\frac{d\alpha}{dT}\right) = \ln(A) + \ln[f(\alpha)] - \frac{E_a}{RT} \tag{9}$$

For a specific conversion at different heating rates, the straight line obtained by ln[β(dα/dT)] vs 1/T plot provides the activation energy through the slope, while the pre-exponential factor (A) is obtained from its intercept.

2.6.4 Master Plot Modified Method

Criado method [29, 30] has been used to estimate the theoretical solid-state reaction mechanism based on Eq. 10, where $x = Ea/RT$ and π(x) approximates the temperature integral which cannot be expressed in a simple analytical form. To reduce the computational errors, the Senum-Yang approximation was used in this study, which is lower than 10^{-5}% when x > 20. The experimental curve can be defined by Eq. 10 and 11, where P(x) is expressed by Eq. 12 [31], where f(α) and g(α) are different solid-state reaction models shown in Table 1 [32].

$$Z(\alpha) = \frac{d\alpha/dt}{\beta}\pi(x)T \tag{10}$$

$$Z(\alpha) = \frac{d\alpha E_a}{dtR}e^{\left(\frac{-E_a}{RT}\right)}P(x) \tag{11}$$

$$P(x) = \frac{e^{-x}}{x}\cdot\frac{x^3 + 18x^2 + 86x + 96}{x^4 + 20x^3 + 120x^2 + 240x + 120} \tag{12}$$

To increase the accuracy of determining the decomposition mechanism, the algebraic equation derived from the Pythagorean Theorem (Eq. 14) is used to measure the distance between two points in a Cartesian plane, since the x-axis is shared by both experimental and master curves. The master plot as a function of conversion (α) can be obtained by Eq. 13, where $x_b = x_a$ represents the x coordinate of the master plot and the experimental curve, related to conversion (α). y_b represents the y coordinate $Z(\alpha)\Big/_{Z(0.5)}$ of the experimental curve and y_a represents the y-axis coordinate $g(\alpha)\Big/_{g(0.5)}$ of the master curves. Eq. 14 was applied to all experimental curves compared to the master plot under study, with the nearest distance value of 0 (zero) modeling the reaction for a specific conversion (α).

$$Z(\alpha) = f(\alpha)\cdot g(\alpha) \tag{13}$$

$$d = \sqrt{(x_b - x_a)^2 + (y_b - y_a)^2} \tag{14}$$

2.6.5 Thermodynamic Parameters

The thermodynamic parameters were obtained from Eq. 15, 16 and 17, where K_b, *h* and T_m represent the Boltzmann constant (1.381 × 10^{-23} J K^{-1}), Plank constant (6.626 × 10^{-34} J s) and DTG (derivative thermogravimetry) peak temperature, respectively.

$$\Delta H = Ea - RT \tag{15}$$

$$\Delta G = E_a + RT_m \ln\left(\frac{K_b T_m}{hA}\right) \tag{16}$$

$$\Delta S = (\Delta H - \Delta G)/T_m \tag{17}$$

3. Results

3.1 Catalysts Characterization

The formation of the beta zeolite was confirmed by X-ray diffraction. For all cases (Figure S1), peaks at 8° and 22° were detected, which are characteristic of the zeolite structure [9, 10]. All samples showed the same X-ray diffraction pattern and those containing nickel showed an increase in intensity at 44°, due to the overlap of nickel and zeolite peaks. The results of the chemical analysis of the catalysts were shown in Table S1. It can be noted that the values of the Si/Al ratio decreased slightly due to the addition of nickel, regardless of its content, indicating a loss of aluminum during the incorporation of nickel. Also, nickel contents were higher than expected, indicating that some zeolite was lost during nickel impregnation. In addition, the samples showed high specific surface areas, which is consistent with previous work [9]. After nickel impregnation, no change in this parameter was noted and the observed differences were within the experimental error.

3.2 Thermogravimetry Analysis

Figure 1 showed the TG and DTG curves, whose profiles were typical of both catalytic and non-catalytic pyrolysis for lignocellulosic materials. Two main weight losses and a pseudo stationary decomposition as the third stage can be noted [33, 34], which extended to the end of the analysis. Moreover, as the heating rate increased, the curves were shifted to higher temperatures, regardless of the catalyst. This finding may be related to the thermal hysteresis in the heat transfer and kinetic of MDF pyrolysis at different heating rates. Furthermore, higher heating rates decreased resistance to heat and mass transfer, thereby providing energy for endothermic reactions [35]. The first stage occurs from the beginning of analysis to approximately 130°C and corresponds to volatile compounds associated with the residual nitrogenated components from MDF treatment [36] and adsorbed water. As shown in Table 2, the values were similar among the samples regardless of the catalyst, which illustrates the results obtained at 10°C min^{-1}. The second stage is more pronounced and can be considered the main decomposition event since the biomass components are decomposed in this temperature range. It starts around 200°C and rises to 430°C, comprising a conversion fraction range (α) of around ≈10-85%. It is related to the decomposition of hemicellulose (200-350°C), cellulose (300-375°C) and lignin (250-500°C) [20, 37]. At this temperature range, biomass has enough energy to break the bonds of C=O, -OH and C=C long chain to produce liquid and gaseous primary products such as water, carbon monoxide and carbon dioxide [35, 38]. Other products are produced in this step, mainly those associated with lower molecular weight hydrocarbon chains, from the breaking of side chains and of α- and β-aryl-alkyl-ether [39, 40]. In this range, the highest conversion was observed for the MB3Ni sample, as shown in Table 2.

Table 2 Temperature ranges (°C) and weight losses (%) of samples during MDF pyrolysis at heating rate β = 10°C min^{-1}.

Samples	Stage I		Stage II		Stage III	
	(°C)	(%)	(°C)	(%)	(°C)	(%)
M	25.0-114.0	6.82	114.0-413.6	69.32	413.6->900	20.08
MB	25.0-102.8	6.55	102.8-416.3	71.15	416.3-763.7	12.72

MB3Ni	25.0-94.3	6.12	94.3-413.6	74.12	413.6-758.2	18.85
MB5Ni	25.0-114.0	7.43	114.0-419.1	68.77	419.1-761.0	16.86

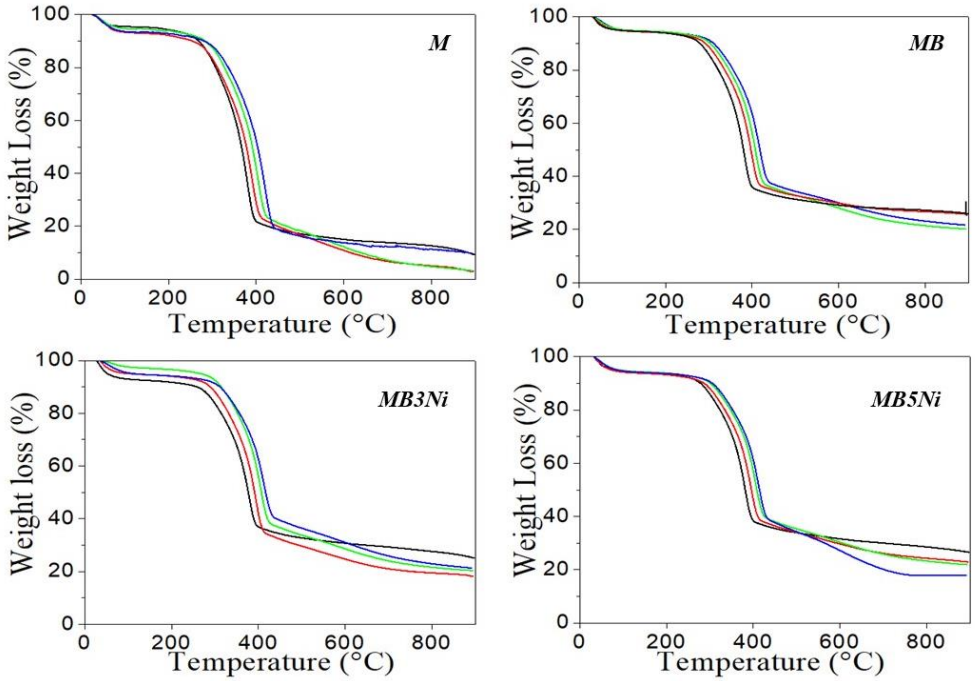

Figure 1 TG profiles of (a) M, (b) MB, (c) MB3Ni and (d) MB5Ni samples at β heating rates: (▪)5, (▪)10, (▪)15 e (▪) 20°C min^{-1}.

The weight losses were better shown in DTG curves (Figure 2), in which the maximum conversion rate was related to the second decomposition step. The peaks occur in the same temperature range for the different samples. The catalyst slightly shifted the DTG peak to higher temperatures compared to non-catalytic pyrolysis, suggesting a change in the reaction pathways. As found by Mayer *et al.* (2022), studied the MDF decomposition over beta zeolite obtained from commercial silica, catalytic pyrolysis produced mostly high-value aromatics (benzene, toluene, xylenes and ethylbenzene), whereas non-catalytic pyrolysis produced only oxygenated compounds [9]. the DTG peak temperatures of the samples were summarized in Table 2.

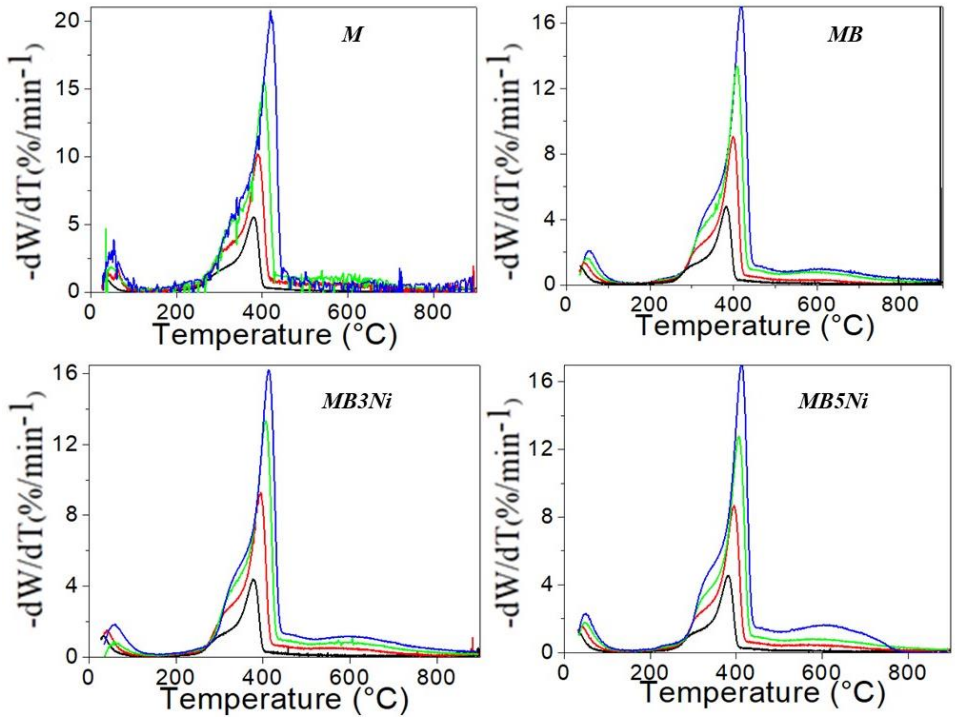

Figure 2 DTG profiles of samples (a) M, (b) MB, (c) MB3Ni and (d) MB5Ni at heating rates β: (▪)5, (▪)10, (▪)15 e (▪) 20°C min^{-1}.

As shown in Figure 2, the MDF decomposition rate increases with the heating rate and the temperature range remain constant, indicating an increased gas and volatile production. This tendency is observed for all samples regardless of the catalyst. The third decomposition stage (Figure 1 and Figure 2) is related to other products, such as biochar mainly formed at low heating rates. This condition causes low weight losses close to thermal stability and can be considered as a pseudo-steady state. In this step, some rearrangement reactions occur, such as the production of free radicals, bond breakage and secondary products [41]. Table 2 summarizes the temperature ranges and weight losses for MDF catalytic and non-catalytic pyrolysis at a heating rate (β) of 10°C min^{-1}. For catalytic pyrolysis, the pseudo-steady stage was reached at around 760°C, indicating the end of MDF decomposition while for non-catalytic pyrolysis, the weight loss continued until the end of the analysis.

The data from Table 3 show that MB3Ni produced the lowest residue amount among the samples, followed by non-catalytic pyrolysis, MB5Ni and MB. The highest amount occurred over beta zeolite, probably related to its high acidity that favors cracking and biochar formation (9,10). Nickel addition decreases the amount of Brønsted acid sites (BAS) [9] and then reduces the biochar production. It can be observed that the amount of residue over beta zeolite was higher than that noted for non-catalytic pyrolysis, indicating an increased polymerization reaction for biochar production due to the high internal and external acidity of the beta zeolite catalyst. In a previous work [9] it has been found that beta zeolite significantly decreased the O-content in the products due to the optimized properties of the catalyst, such as high specific surface area, strong BAS and LAS (Lewis acid sites) and large pores.

Table 3 Maximum MDF decomposition temperature (Tm) and biochar produced during pyrolysis (β = 10°C min^{-1})

Sample	Tm (°C)	MDF weight loss (%)	Biochar (%)
M	389.4	96.97	3.03
MB	398.8	88.95	11.05
MB3Ni	395.0	98.10	1.90
MB5Ni	395.3	92.40	7.60

Furthermore, the large pore size facilitates the diffusion of compounds into the channel structure, leading to cracking, deoxygenation/hydrodeoxygenation, hydrogenation/dehydrogenation, and other reactions in the internal acidic sites. However, the large pores also increase the formation of polyaromatic hydrocarbons (PAH) on the acidic sites of the catalyst, which increase the formation of biochar and consequently lead to the catalyst deactivation. Without any catalyst, the amount of decomposed MDF is high but the products are only oxygenated compounds found in previous work [9]. On the other hand, although the amount decomposed on beta zeolite was lower, there was an advantage that less oxygenated compounds were formed. Moreover, BTEX, other monoaromatics, polyaromatics and naphthalene were produced. The addition of nickel to beta zeolite increased the maximum decomposed MDF and decreased the amount of oxygenated compounds even more. It was reported [9] that nickel oxide entered a reduced state during pyrolysis, producing metallic nickel species which will cooperate with the acidic sites of zeolites to produce BTEX and other compounds. In addition, the amount of toxic PAH was decreased and reached trace levels on MB5Ni. Over the MB3Ni sample, the highest maximum decomposed MDF and the lowest amount of oxygenated products and PAH were detected, besides the highest amount of BTEX.

3.3 Kinetic Study

The activation energy and pre-exponential factor were calculated at each conversion step from the slopes and intercepts of plots shown in Figure S2. The activation energies and the logarithm of pre-exponential factor obtained from the different methods are shown in Table 4. It can be noted that activation energy values have small fluctuations in the conversion range (α = 0.2-0.8) regardless of the method used. They are related to complex multi-step reactions such as competitive, parallel, and successive reactions occurring during pyrolysis [32]. These results are illustrated in Figure 3, where these variations can be better visualized. The values follow the same trend for all models as α increases from 0.2 to 0.7. However, when α reached 0.7 from 0.8 values a decrease in E_a was observed at around 420°C, where the maximum decomposition of biomass occurred (Figure 2). These results were in agreement with those found by Aslan *et al.* (2018) who used DAEM model to obtain thermokinetic parameters of MDF pyrolysis using TGA data [37].

Table 4 Activation energies (E_a) for MDF pyrolysis catalysts calculated by Flynn-Wall-Ozawa (FWO), Kissinger-Akira-Sunose (KAS) and Friedman (F) isoconversional methods. R^2 is the correlation coefficient for each method.

Activation Energy (E_a) – kJ mol^{-1}												
α	**M**						**MB**					
	FWO	**R^2**	**KAS**	**R^2**	**F**	**R^2**	**FWO**	**R^2**	**KAS**	**R^2**	**F**	**R^2**
0.2	120.34	0.9272	116.80	0.9155	116.30	0.9286	101.32	0.9877	96.71	0.9850	96.43	0.9861
0.3	123.58	0.9666	119.78	0.9607	119.39	0.9693	104.37	0.9887	99.58	0.9865	99.85	0.9877
0.4	127.44	0.9865	123.49	0.9841	123.38	0.9894	109.43	0.9917	104.44	0.9899	104.99	0.9910
0.5	128.22	0.9926	124.06	0.9913	124.03	0.9948	115.55	0.9946	110.63	0.9934	111.37	0.9944
0.6	127.90	0.9933	123.56	0.9920	123.82	0.9951	118.77	0.9954	113.86	0.9944	114.86	0.9955
0.7	128.68	0.9968	124.21	0.9961	124.41	0.9980	118.32	0.9950	113.24	0.9938	114.29	0.9949
0.8	100.61	0.8475	94.49	0.8157	94.94	0.9953	84.39	0.9441	77.29	0.9272	78.48	0.9953
Average	**122.40**	**0.9586**	**118.06**	**0.9501**	**118.04**	**0.9815**	**107.45**	**0.9853**	**102.25**	**0.9658**	**102.90**	**0.9921**
	MB3Ni						**MB5Ni**					
	FWO	**R^2**	**KAS**	**R^2**	**F**	**R^2**	**FWO**	**R^2**	**KAS**	**R^2**	**F**	**R^2**
0.2	76.20	0.9746	70.36	0.9673	71.86	0.9694	103.97	0.9869	99.51	0.9841	99.23	0.9864
0.3	87.34	0.9897	81.60	0.9870	83.65	0.9881	107.77	0.9905	103.03	0.9884	103.20	0.9902
0.4	97.46	0.9966	91.91	0.9957	94.40	0.9961	113.71	0.9938	108.93	0.9924	109.46	0.9938
0.5	106.82	0.9985	101.50	0.9982	104.33	0.9982	120.87	0.9952	116.24	0.9942	117.04	0.9955
0.6	112.03	0.9986	106.80	0.9983	109.96	0.9981	124.70	0.9958	120.10	0.9949	120.92	0.9961
0.7	111.81	0.9982	106.42	0.9977	109.44	0.9972	120.72	0.9952	115.76	0.9941	116.80	0.9951
0.8	53.62	0.9531	44.61	0.9983	46.77	0.9982	50.28	0.9393	40.97	0.8996	42.36	0.9959
Average	**92.18**	**0.9870**	**86.17**	**0.9918**	**88.63**	**0.9922**	**106.00**	**0.9852**	**100.65**	**0.9782**	**101.29**	**0.9933**

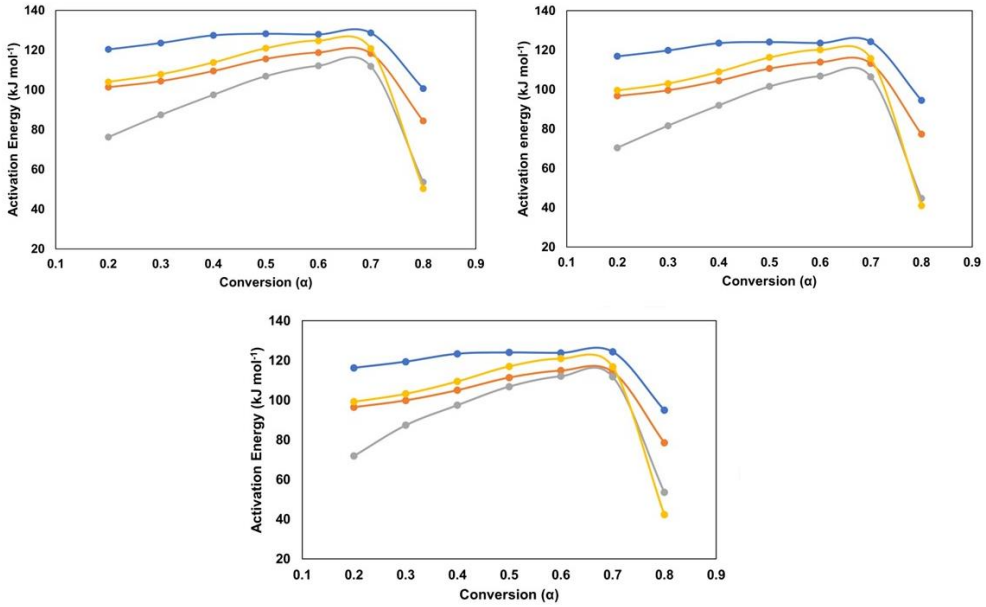

Figure 3 Activation energy change versus conversion rate for (-) M, (-) MB, (-) MB3Ni and (-) MB5Ni samples.

The correlation coefficients obtained from all three methods showed high values, indicating the suitability of the experimental data. Friedman method resulted in the highest values for all samples because it considers the conversion rate in addition to the temperature for each conversion. This provides greater accuracy for this method to respond to infinitesimal variations in conversion, despite the kinetic parameters provided being independent of the reaction model [42]. This is why we have chosen the Friedman method.

As expected, the catalysts decreased the activation energy, with an even greater reduction in nickel. For all methods, the activation energies followed the following order: MB3Ni < MB < MB5Ni < M (Figure 3). For the Friedman method, the activation energy reduction in comparison with non-catalytic pyrolysis (118.04 kJ mol^{-1}) was 15.14 kJ mol^{-1}, 29.41 kJ mol^{-1} and 16.75 kJ mol^{-1} for MB (102.90 kJ mol^{-1}), MB3Ni (88.63 kJ mol^{-1}) and MB5Ni (101.29 kJ mol^{-1}) respectively. As demonstrated by Mayer *et al.* (2022), the non-catalytic pyrolysis of MDF generated large amounts of oxygenated compounds (76.01%) and low amounts of mono or polyaromatic compounds. However, when performed over beta zeolite, the pyrolysis produced more aromatic compounds, especially BTEX increased of 39.35%, 38.65% and 23.51% for beta zeolite impregnated with 3% (B3Ni) and 5% (B5Ni) nickel and nickel-free catalysts, respectively. Furthermore, the order of reduction in the amount of oxygenated compounds was B (0.64%) < B5Ni (2.64%) < B3Ni (14.16%) [9]. Therefore, we can conclude that the reaction pathway provided by the catalysts promotes the production of non-oxygenated aromatic compounds, which involves lower activation energy. In addition, Bienik et al. (2022) investigated the MDF decomposition under argon atmosphere using the Friedman, FWO and KAS methods [43]. The authors found activation energy values significantly higher ($E_{a_{\mathrm{Friedman}}}$: 216.7 kJ mol^{-1}, $E_{a_{\mathrm{KAS}}}$: 198.2 kJ mol^{-1} and $E_{a_{\mathrm{FWO}}}$: 197.9 kJ mol^{-1}) than those found in our work for all conversion ranges (α). The Friedman method also showed the best fit, in agreement with our work. The differences between the results of the two works may be associated with the pre-treatment we have done, since many toxic compounds have been removed, eliminating their reaction during

pyrolysis which then affects the global activation energy [9]. They probably decomposed and/or reacted during pyrolysis affecting the kinetic parameters. The introduction of nickel as an active phase in the catalyst promotes a change in the chemical environment, modifying the amount and strength of acid sites, in addition to favoring cracking/hydrocracking, hydrogenation/dehydrogenation and isomerization reactions, producing aromatic compounds [9]. However, this change did not cause a significant decrease in activation energy, except for B3Ni sample.

Criado model-fit master plots were used to determine the theoretical reaction mechanism that best describes the solid phase processes of MDF pyrolysis and the curves are shown in Figure S2. The non-catalytic pyrolysis showed a better fit to the one-dimensional interface reaction mechanism (R1), which describes a model in which the decomposition depends on the reaction rate, controlled both by the progression of interface reaction towards the crystal center or by the rate conversion raised to a power (fractional or integral), which is the reaction order [43]. On the other hand, the mechanism for catalytic pyrolysis was different, showing the best fit by the two-dimensional diffusion model (D2). In this case, the rate of product formation decreased with the increasing thickness of the product barrier layer. In addition, the solid particles were assumed to be cylindrical and diffusion occurs radially through a cylindrical shell with an increasing reaction zone, indicating the influence of geometric particles [44, 45].

To determine the pre-exponential factor from the integral isoconversional models, it is necessary to know the model solid-state reaction [f(α)], and the y-intercept. Table S2 shows the observed pre-exponential factor for pyrolysis and Figure 4 shows the values of the pre-exponential factor, the value was expressed as $\log_{10}(A)$ to show more comprehensive values. It can be noted that the value varies to a large extent with conversion and also among the samples.

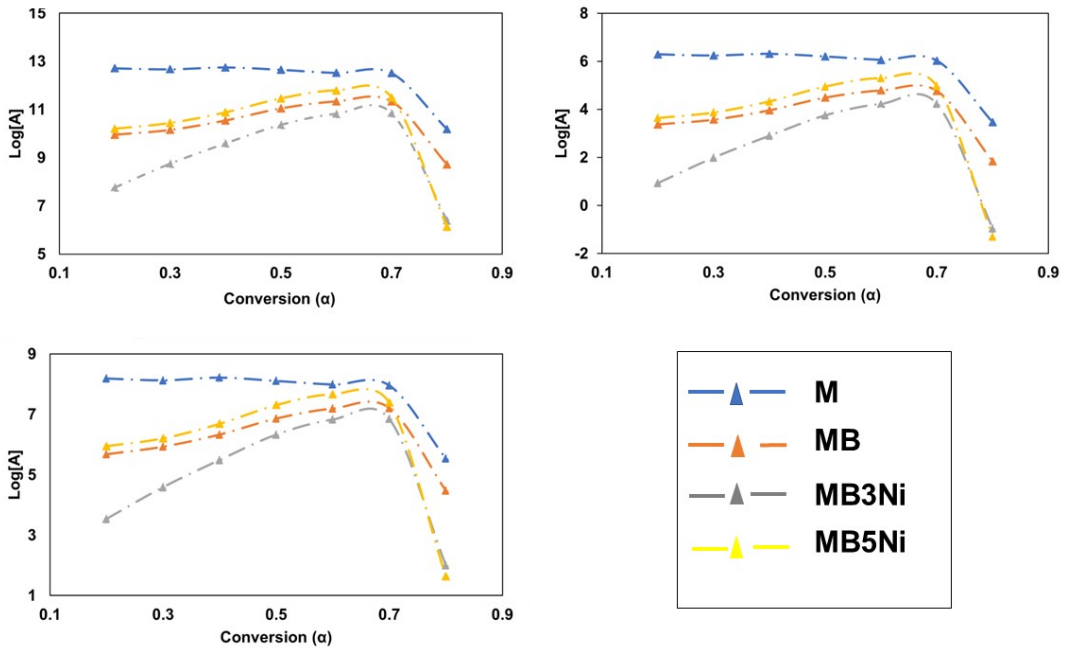

Figure 4 $\text{Log}_{10}(A)$ versus conversion (α) for catalytic and non-catalytic pyrolysis using FWO, KAS and Friedman models.

Thermodynamic parameters obtained using Friedman model are displayed in Table 5. The Gibbs free energy (ΔG) is a parameter that determines the spontaneity of reactions, in addition to the direction and degree of chemical reactions that occur during a process. The values showed small differences for catalytic and non-catalytic pyrolysis in the order $\Delta G_M < \Delta G_{MB5Ni} \approx \Delta G_{MB} < \Delta G_{MB3Ni}$. This may be related to the different pathways provided by the different catalysts, some reactions that occur too slowly on the catalysts are suppressed.

Table 5 Evaluation of thermodynamic parameters of catalytic and non-catalytic systems.

	ΔG (kJ mol^{-1})	**ΔH (kJ mol^{-1})**	**ΔS (10^2) (kJ mol^{-1} K)**
M	189.55	120.07	-1.05
MB	191.86	97.45	-1.41
MB3Ni	192.36	88.72	-1.54
MB5Ni	191.63	101.29	-0.14

These evaluation values were higher than those obtained by Aslan et al. for MDF pyrolysis, which ranged from 147.87 and 169.20 kJ mol^{-1} with a calculated mean value of 175.29 kJ mol^{-1} [37]. The differences among the values suggested the role of catalysts and the MDRF pre-treatment in affecting the reaction network, resulting in different thermodynamics parameters. Table S3 presents Gibbs free energy, enthalpy and entropy values for each conversion fraction (α) studied.

Enthalpy (ΔH) is also a significant thermodynamic state function of a chemical reaction that reflects the endothermic or exothermic behavior of reactions. Enthalpy values also changed among the samples, showing the following order: $\Delta H_{MB3Ni} < \Delta H_{MB} < \Delta H_{MB5Ni} < \Delta H_M$, indicating a less endothermic global process for MB3Ni.This suggested that more exothermic reactions were favored over this catalyst compared to the others. The negative entropy values are consistent with the Gibbs free energy, indicating that pyrolysis decreases the freedom degree of biomass higher than its products. Therefore, MDF pyrolysis is a global non-spontaneous and endothermic process.

4. Conclusions

The use of catalysts based on beta zeolite and zeolite-supported nickel in MDF pyrolysis promoted a reduction in activation energy throughout the process. The 3% nickel catalyst led to the lowest activation energy, probably due to the synergy between the metal and zeolite, which reduces the BAS sites that promote the deoxygenation of compounds. The activation energy following the order: $E_{aMB3Ni} < E_{aMB} < E_{aMB5Ni} < E_{aM}$.

The theoretical mechanism reaction obtained by Criado master-plots showed that catalytic and non-catalytic processes had different mechanisms. In the last case, the two-dimensional diffusion model (D2) was the most suitable to describe MDF decomposition. According to this model, the rate of product formation was decreased with increasing thickness of the production barrier layer. For non-catalytic process, the MDF decomposition depended on the reaction rate, controlled both by the progression of the reaction interface towards the crystal center and the increase in the conversion of the reactants to a power (fractional or integral) which is the reaction order.

MDF pyrolysis has been proven to be a non-spontaneous and endothermic global process in each. The Gibbs free energy was nearly the same, but enthalpy and entropy changed among the samples. This finding may be related to the different reactions occurring without catalyst and on different catalysts.

Acknowledgments

The authors thank Financiadora de Estudos e Projetos (FINEP) and Conselho Nacional de Desenvolvimento Científico e Tecnológico (CNPq) for lhe financial support. MO acknowledgs CAPES for his graduate scholarship.

Author Contributions

Mateus Carvalho: Conceptualization, Investigation, Calculations, Writing – Original Draft, Data Curation, Visualization, Editing final manuscript. **Ana Paula Oliveira, Francieli Mayer, Cesário Virgens**: Supervision, Review & Editting. **Maria do Carmo Rangel**: Conceptualization, Supervision, Review & Editing.

Funding

This study was financed in part by the Coordenação de Aperfeiçoamento de Pessoal de Nível Superior - Brazil (CAPES), Financiadora de Estudos e Projetos (FINEP) and Conselho Nacional de Desenvolvimento Cinetífico e Tecnológico (CNPq).

Competing Interests

The authors have declared that no competing interests exist.

Additional Materials

The following additional materials are uploaded at the page of this paper.

1. Figure S1: X-ray diffractogram of zeolite beta impregnated with 5% nickel.
2. Table S1: Silicon, aluminum and nickel contents and specific surface areas and porosity of the catalysts. B = beta zeolite; B3Ni = beta zeolite impregnated with 3% nickel and B5Ni = beta zeolite impregnated with 3% nickel and SU = grape residues without catalyst.
3. Figure S2: Kinetic curves at different conversion degrees for FWO, KAS and Friedman methods for MDF catalytic and non-catalytic pyrolysis. The lines presented are associated to conversion fraction (a): (-)0.2; (-)0.3; (-)0.4; (-)0.5; (-)0.6; (-)0.7 and (-)0.8.
4. Figure S3: Master curves and experimental data obtained using the Criado method for M, MB, MB3Ni and MB5Ni.
5. Table S2: Pre-exponential factor (A) for MDF pyrolysis over the catalysts calculated by Friedman (F), Kissinger-Akira-Sunose (KAS) and Flynn-Wall-Ozawa (FWO) isoconversional methods. The results were presented in $\log_{10}$ to facilitate data manipulation.
6. Table S3: Thermodynamic parameters for evaluated catalytic and non-catalytic systems for each conversion fraction studied.

References

1. Zhu QL, Wu B, Pisutpaisal N, Wang YW, Ma Kd, Dai LC, et al. Bioenergy from dairy manure: Technologies, challenges and opportunities. Sci Total Environ. 2021; 790: 148199.
2. Okolie JA, Mukherjee A, Nanda S, Dalai AK, Kozinski JA. Next-generation biofuels and platform biochemicals from lignocellulosic biomass. Int J Energy Res. 2021; 45: 14145-14169.
3. Dey S, Reang NM, Das PK, Deb M. A comprehensive study on prospects of economy, environment, and efficiency of palm oil biodiesel as a renewable fuel. J Clean Prod. 2021; 286: 124981.
4. Briones-Hidrovo A, Copa J, Tarelho LAC, Gonçalves C, Pacheco da Costa T, Dias AC. Environmental and energy performance of residual forest biomass for electricity generation: Gasification vs. Combustion. J Clean Prod. 2021; 289: 125680.
5. Dutta S. Hydro(deoxygenation) reaction network of lignocellulosic oxygenates. ChemSusChem. 2020; 13: 2894-2915.
6. Vickers NJ. Animal communication: When I'm calling you, will you answer too? Curr Biol. 2017; 27: R713-R715.
7. Robinson AM, Hensley JE, Medlin JW. Bifunctional catalysts for upgrading of biomass-derived oxygenates: A review. ACS Catal. 2016; 6: 5026-5043.
8. Jae J, Tompsett GA, Foster AJ, Hammond KD, Auerbach SM, Lobo RF, et al. Investigation into the shape selectivity of zeolite catalysts for biomass conversion. J Catal. 2011; 279: 257-268.
9. Mayer FM, de Oliveira APS, de Oliveira Junior DL, Agustini BC, da Silva GA, Tanabe EH, et al. Influence of nickel modified Beta zeolite in the production of BTEX during analytical pyrolysis of medium-density fiberboard (MDF). Waste Biomass Valorization. 2022; 13: 1717-1729.
10. de Tarso Figueiredo Grecco S, de Carvalho DR, Zandonai CH, Fernandes-Machado NRC, Lião LM, Urquieta-González EA, et al. Catalytic cracking of crude soybean oil on Beta nanozeolites. J Mol Catal A Chem. 2016; 422: 89-102.
11. Rahman MM, Liu R, Cai J. Catalytic fast pyrolysis of biomass over zeolites for high quality bio-oil – A review. Fuel Process Technol. 2018; 180: 32-46.
12. Liu SN, Cao JP, Zhao XY, Wang JX, Ren XY, Yuan ZS, et al. Effect of zeolite structure on light aromatics formation during upgrading of cellulose fast pyrolysis vapor. J Energy Inst. 2019; 92: 1567-1576.
13. Yu Y, Li X, Su L, Zhang Y, Wang Y, Zhang H. The role of shape selectivity in catalytic fast pyrolysis of lignin with zeolite catalysts. Appl Catal A Gen. 2012; 447-448: 115-123.
14. Pattiya A. 2 - Catalytic pyrolysis. In: Direct thermochemical liquefaction for energy applications. Woodhead Publishing; 2018. pp. 29-64.
15. Balagurumurthy B, Singh R, Bhaskar T. Chapter 4 - Catalysts for thermochemical conversion of biomass. In: Recent advances in thermo-chemical conversion of biomass. Boston: Elsevier; 2015. pp. 109-132.
16. Santos DBP, de Jesus MF, Júnior JMF, de Moraes Pires CA. Determination of kinetic parameters for the sisal residue pyrolysis through thermal analysis. J Ind Eng Chem. 2022; 109: 296-305.
17. das Virgens CF, Castro JDS. Screening of slow pyrolysis routes for maximum biofuel production from Syzygium malaccense biomass by TGA-FSD and chemometric tools. J Therm Anal Calorim. 2021; 146: 2005-2014.

18. Vuppaladadiyam AK, Memon MZ, Ji G, Raheem A, Jia TZ, Dupont V, et al. Thermal characteristics and kinetic analysis of woody biomass pyrolysis in the presence of bifunctional alkali metal ceramics. ACS Sustain Chem Eng. 2019; 7: 238-248.
19. Volli V, Gollakota ARK, Shu CM. Comparative studies on thermochemical behavior and kinetics of lignocellulosic biomass residues using TG-FTIR and Py-GC/MS. Sci Total Environ. 2021; 792: 148392.
20. das Virgens CF, Carneiro LL, da Silva EGP, das Chagas TP. Prediction of alkaline treatment effect on the slow pyrolysis of the Pachira aquatica Aubl. Fruit bark using artificial neural networks. Braz J Develop. 2020; 6: 79686-79704.
21. Castro JDS, da Silva EGP, Virgens CF. Evaluation of models to predict the influence of chemical pretreatment on the peels of Nephelium lappaceum L. Based on pyrolysis kinetic parameters obtained using a combined Fraser-Suzuki function and Friedman's isoconversional method. J Anal Appl Pyrolysis. 2020; 149: 104827.
22. Vaudry F, Di Renzo F, Espiau P, Fajula F, Schulz P. Aluminum-rich zeolite beta. Zeolites. 1997; 19: 253-258.
23. Ozawa T. A new method of analyzing thermogravimetric data. Bull Chem Soc Jpn. 1965; 38: 1881-1886.
24. Flynn JH, Wall LA. General treatment of the thermogravimetry of polymers. J Res Natl Bur Stand A Phys Chem. 1966; 70A: 487-523.
25. Kissinger HE. Variation of peak temperature with heating rate in differential thermal analysis. J Res Natl Bur Stand. 1956; 57: 217-221.
26. Zhang X. Applications of kinetic methods in thermal analysis: A review. Eng Sci. 2020; 14: 1-13.
27. Pérez JM, Oliet M, Alonso MV, Rodríguez F. Cure kinetics of lignin–novolac resins studied by isoconversional methods. Thermochim Acta. 2009; 487: 39-42.
28. Friedman HL. Kinetics of thermal degradation of char-forming plastics from thermogravimetry. Application to a phenolic plastic. J Polym Sci Part C Polym Symp. 1964; 6: 183-195.
29. Criado JM, Málek J, Ortega A. Applicability of the master plots in kinetic analysis of non-isothermal data. Thermochim Acta. 1989; 147: 377-385.
30. Sánchez-Jiménez PE, Pérez-Maqueda LA, Perejón A, Criado JM. Generalized master plots as a straightforward approach for determining the kinetic model: The case of cellulose pyrolysis. Thermochim Acta. 2013; 552: 54-59.
31. Pérez-Maqueda LA, Criado JM. The accuracy of Senum and Yang's approximations to the Arrhenius integral. J Therm Anal Calorim. 2000; 60: 909-915.
32. Patidar K, Singathia A, Vashishtha M, Kumar Sangal V, Upadhyaya S. Investigation of kinetic and thermodynamic parameters approaches to non-isothermal pyrolysis of mustard stalk using model-free and master plots methods. Mater Sci Energy Technol. 2022; 5: 6-14.
33. Hu M, Chen Z, Wang S, Guo D, Ma C, Zhou Y, et al. Thermogravimetric kinetics of lignocellulosic biomass slow pyrolysis using distributed activation energy model, Fraser–Suzuki deconvolution, and iso-conversional method. Energy Convers Manag. 2016; 118: 1-11.
34. Kabir G, Hameed BH. Recent progress on catalytic pyrolysis of lignocellulosic biomass to high-grade bio-oil and bio-chemicals. Renew Sustain Energy Rev. 2017; 70: 945-967.
35. Guedes RE, Luna AS, Torres AR. Operating parameters for bio-oil production in biomass pyrolysis: A review. J Anal Appl Pyrolysis. 2018; 129: 134-149.

36. Mayer FM, Teixeira CM, Andrade Pacheco JG, de Souza CT, de Vila Bauer D, Caramão EB, et al. Characterization of analytical fast pyrolysis vapors of medium-density fiberboard (mdf) using metal-modified HZSM-5. J Anal Appl Pyrolysis. 2018; 136: 87-95.
37. Aslan DI, Özoğul B, Ceylan S, Geyikçi F. Thermokinetic analysis and product characterization of medium density fiberboard pyrolysis. Bioresour Technol. 2018; 258: 105-110.
38. Minh Loy AC, Yusup S, Fui Chin BL, Wai Gan DK, Shahbaz M, Acda MN, et al. Comparative study of in-situ catalytic pyrolysis of rice husk for syngas production: Kinetics modelling and product gas analysis. J Clean Prod. 2018; 197: 1231-1243.
39. Collard FX, Blin J. A review on pyrolysis of biomass constituents: Mechanisms and composition of the products obtained from the conversion of cellulose, hemicelluloses and lignin. Renew Sustain Energy Rev. 2014; 38: 594-608.
40. Poveda-Giraldo JA, Solarte-Toro JC, Cardona Alzate CA. The potential use of lignin as a platform product in biorefineries: A review. Renew Sustain Energy Rev. 2021; 138: 110688.
41. Açıkalın K. Determination of kinetic triplet, thermal degradation behaviour and thermodynamic properties for pyrolysis of a lignocellulosic biomass. Bioresour Technol. 2021; 337: 125438.
42. Rico JJ, Pérez-Orozco R, Patiño Vilas D, Porteiro J. TG/DSC and kinetic parametrization of the combustion of agricultural and forestry residues. Biomass Bioenergy. 2022; 162: 106485.
43. Khawam A, Flanagan DR. Solid-state kinetic models: Basics and mathematical fundamentals. J Phys Chem B. 2006; 110: 17315-17328.
44. Koga N, Tanaka H. A physico-geometric approach to the kinetics of solid-state reactions as exemplified by the thermal dehydration and decomposition of inorganic solids. Thermochim Acta. 2002; 388: 41-61.
45. Liu F, Sommer F, Bos C, Mittemeijer EJ. Analysis of solid state phase transformation kinetics: Models and recipes. Inter Mater Rev. 2007; 52: 193-212.